A&A, 711, A229 (2026)
https://doi.org/10.1051/0004-6361/202660788

Astronomy & Astrophysics

Dynamical analysis of the 5:1 mean-motion resonance of the HD 202206 system

Yingyi Cao[1,⋆], Man Hoi Lee[1,2,3], Sabine Reffert[4], Trifon Trifonov[4,5], and Stefan Stefanov[5,6]

[1] Department of Earth and Planetary Sciences, The University of Hong Kong, Pokfulam Road, Hong Kong
[2] Department of Physics, The University of Hong Kong, Pokfulam Road, Hong Kong
[3] Hong Kong Institute for Astronomy and Astrophysics, Hong Kong
[4] Landessternwarte, Zentrum für Astronomie der Universität Heidelberg, Königstuhl 12, 69117 Heidelberg, Germany
[5] Department of Astronomy, Faculty of Physics, Sofia University "St Kliment Ohridski", 5 James Bourchier Blvd, 1164 Sofia, Bulgaria
[6] Institute of Astronomy and National Astronomical Observatory, Bulgarian Academy of Sciences, Tsarigradsko Shose 72, 1784 Sofia, Bulgaria

Received 5 May 2026 / Accepted 23 June 2026

ABSTRACT

Context. The HD 202206 system, which features two substellar companions with a 5:1 period ratio around a solar-type star, offers a rare opportunity to study high-order mean-motion resonances and provides new insights into the formation and evolution of substellar companions in extrasolar planetary systems.

Aims. We revisited the HD 202206 system, aiming to conduct a more comprehensive analysis of orbital inclinations, companion masses, resonance dynamics, and potential formation mechanisms.

Methods. Our analysis of the astrometric jitter around the best fit in the *Gaia* DR3 catalog and the proper motion anomalies between HIPPARCOS and *Gaia* places robust constraints on the orbital inclinations. We performed a new dynamical fit to all available radial velocity data from the CORALIE and HARPS spectrographs. We assessed the dynamical configuration and long-term stability of the system using samples generated by nested sampling.

Results. Our analysis shows that the orbital inclinations are strongly constrained to about 51°. Consequently, the best-fit dynamical solution, assuming a coplanar and inclined ($i = 51°$) configuration, yields an inner brown dwarf of 21.56 M_J and an outer giant planet of 3.12 M_J. The corresponding orbital periods are 256.26 days and 1298.87 days, with eccentricities of 0.426 and 0.180. An investigation of the five relevant resonance angles shows that only one is librating with a large amplitude. Our stability analysis confirms that the system is dynamically stable.

Conclusions. Our results provide new constraints on the masses and inclination of the system, challenging earlier claims of a face-on configuration and shedding light on the formation and evolution of substellar companions in extrasolar planetary systems.

Key words. methods: data analysis – methods: numerical – techniques: radial velocities – planets and satellites: dynamical evolution and stability

1. Introduction

Mean-motion resonances (MMRs) in extrasolar multi-planet systems offer key insights into their formation and dynamical history. In particular, they provide important constraints on the migration and eccentricity damping induced by planet–disk interactions (Lee & Peale 2002; Kley et al. 2004). Most observed resonant pairs are found in first-order resonances. Well-established examples include GJ 876 (Marcy et al. 2001), HD 82943 (Mayor et al. 2004), HD 73526 (Tinney et al. 2006), η Cet (Trifonov et al. 2014), and HD 27894 (Trifonov et al. 2017) in the 2:1 MMR, as well as HD 45364 in the 3:2 MMR (Correia et al. 2009) and 7 CMa in the 4:3 MMR (Luque et al. 2019).

In contrast, high-order resonances are comparatively rare. Confirmed examples include the 3:1 MMR in HD 60532 (Desort et al. 2008; Laskar & Correia 2009), the 5:1 MMR in HD 202206 (Correia et al. 2005; Couetdic et al. 2010), and the 6:1 MMR in ν Ophiuchi (Sato et al. 2012; Quirrenbach et al. 2019). Several additional systems have been reported with period ratios close to high-order commensurabilities, such as 4:1 in HD 108874 (Vogt et al. 2005), 7:5 in HD 41248 (Jenkins et al. 2013), and 9:7 in the Kepler-29 system (Migaszewski et al. 2016). The scarcity of high-order MMRs likely reflects the increasingly restrictive dynamical conditions required for resonant capture and long-term stability as the resonance order increases, making such configurations more difficult to establish and preserve during planetary migration. These cases challenge standard migration scenarios and help constrain the diversity of disk conditions and dynamical histories (Papaloizou & Terquem 2006).

The inner companion of HD 202206 has a minimum mass ≈17 M_J (where M_J is the mass of Jupiter) and is thus firmly in the brown dwarf regime; the outer companion is a giant planet (Correia et al. 2005; Couetdic et al. 2010). A resonant system that contains both a brown dwarf and a giant planet provides valuable insight into the limits of planet and brown dwarf formation, and into the possibility of a continuous transition between the two populations. Brown dwarfs can form either through fragmentation like low-mass stars or within disks like massive planets, and their coexistence with resonant giant planets offers an important test of these different scenarios (Mordasini et al. 2009; Ma & Ge 2014).

⋆ Corresponding author: astrocyy@connect.hku.hk

Previous studies of HD 202206 have established the dynamical structure around the 5:1 commensurability (Correia et al. 2005; Couetdic et al. 2010). Combining *Hubble* Space Telescope Fine Guidance Sensor astrometry with radial velocities (RVs), Benedict & Harrison (2017) determined orbital inclinations of $i_b = 10.9° \pm 0.8°$ and $i_c = 7.7° \pm 1.1°$ for the inner and outer companions, respectively. This indicates that the system is nearly face on and approximately coplanar, and implies a stellar-mass inner companion and a brown dwarf outer companion.

In this work, we reexamined the inclination and show that a nearly face-on solution is not supported. We refined constraints on the true architecture of HD 202206 and confirmed the substellar nature of the inner companion. The CORALIE and High Accuracy Radial velocity Planet Searcher (HARPS) RV data and the parameters of the host star are provided in Sects. 2 and 3, respectively. In Sect. 4, we present the Keplerian and coplanar dynamical fits derived from the RV data. Then the inclination constraints are detailed, with the inclination of the system constrained to near 51°, and we present the best coplanar $i = 51°$ dynamical fit. The orbital evolution and long-term dynamical stability of the system are examined in Sect. 5. In Sect. 6, we discuss why only one resonant angle is found to librate, as well as the formation and migration scenario for this system. Finally, we summarize our results in Sect. 7.

2. Radial velocity data

The HD 202206 system was discovered in the CORALIE survey (Correia et al. 2005; Couetdic et al. 2010). The CORALIE échelle spectrograph is mounted on the Swiss 1.2-meter *Leonhard Euler* Telescope at La Silla Observatory of the European Southern Observatory (ESO). It has an average measurement precision of ~5 m s^{-1} (Queloz et al. 2000). A total of 92 RV measurements were obtained between 1999 and 2006, with a median internal measurement error of 5.8 m s^{-1}.

We also found 86 RV measurements from the HARPS spectrograph (obtained between 2004 and 2021) in the spectra available in the public ESO archive[1] and extracted via the HARPS-RVBank (Trifonov et al. 2020). HARPS, in operation at the ESO La Silla 3.6m telescope, is a second-generation RV spectrograph that can attain a higher RV precision of ~1 m s^{-1}. These measurements have much smaller internal errors (with a median of 1.0 m s^{-1}) and significantly expand the time span of observations.

Although the CORALIE RV data are less precise, they increase the time span of available observations by more than 4 years. As a result, our analysis of this system was conducted with the combined dataset of the CORALIE and HARPS data. HARPS underwent a fiber exchange in 2015, which introduced a small but significant RV offset between the two epochs. Hence, its observational record is divided into the HARPS-pre and HARPS-post datasets. The HARPS-pre dataset initially consisted of 64 individual RV measurements. Multiple observations obtained on the same night are not statistically independent and may be affected by short-timescale stellar variability and instrumental systematics. To reduce the impact of these effects and to avoid over-weighting densely sampled nights, we computed nightly averaged RVs. This binning reduced the HARPS-pre dataset to 59 independent data points. Similarly, the HARPS-post dataset was reduced from 22 individual measurements to 20 nightly averaged data points. In total, the combined dataset consists of 171 RVs.

[1] https://archive.eso.org/wdb/wdb/adp/phase3_main/form

Table 1. Stellar parameters of HD 202206.

Parameter	Value	Reference
Parallax (mas)	21.9392 ± 0.0275	Gaia DR3$^{(a)}$
$\mu_\alpha \cos\delta$ (mas yr^{-1})	-39.173 ± 0.027	Gaia DR3
μ_δ (mas yr^{-1})	-120.068 ± 0.022	Gaia DR3
V (mag)	8.07 ± 0.01	Tycho-2$^{(b)}$
B (mag)	8.79 ± 0.02	Tycho-2
Stellar type	G2V	This work
$T_{\rm eff}$ (K)	5764.23^{+64}_{-58}	This work
$\log g$ (cgs)	$4.39^{+0.21}_{-0.19}$	This work
[Fe/H]	$0.23^{+0.12}_{-0.13}$	This work
Radius ($R_\odot$)	$1.04^{+0.02}_{-0.02}$	This work
Luminosity ($L_\odot$)	$1.09^{+0.06}_{-0.06}$	This work
Age (Gyr)	$3.94^{+1.28}_{-3.91}$	This work
Mass ($M_\odot$)	$1.06^{+0.07}_{-0.06}$	This work
Distance (pc)	$45.62^{+0.10}_{-0.06}$	This work

Notes. $^{(a)}$Gaia Collaboration (2023); $^{(b)}$Høg et al. (2000).

3. Stellar parameters

HD 202206 (HIP 104903) is a photometrically stable G2V main-sequence star. We derived the stellar properties of HD 202206 by modeling its spectral energy distribution (SED) using the code ARIADNE[2] (Vines & Jenkins 2022). This tool adopts a Bayesian framework and incorporates multiple SED model grids in order to reduce biases associated with individual model choices. It also estimates stellar mass and age via interpolation of MESA Isochrones and Stellar Tracks (MIST; Dotter 2016; Choi et al. 2016). The SED fitting was performed using photometric data from the following bands: GALEX far-UV; Strömgren v, b, and y; Johnson B and V; Tycho B and V; *Gaia* Data Release 2 G, BP, and RP; TESS (Transiting Exoplanet Survey Satellite); 2MASS J, H, and K; and WISE W1 and W2. These measurements were fitted using atmosphere models from PHOENIX v2 (Husser et al. 2013), BT-Settl, BT-NextGegn, BT-Cond (Hauschildt et al. 1999; Allard et al. 2012; Castelli & Kurucz 2003; Kurucz 1993).

We adopted a Gaussian prior on the distance based on the *Gaia* Early Data Release 3 estimate from Bailer-Jones et al. (2021). Interstellar extinction was assigned a uniform prior between zero and the maximum extinction along the line of sight, computed using the Galactic dust maps of Schlafly & Finkbeiner (2011) in the Python package *dustmaps*[3] (Green 2018). For the initial stellar parameters ($T_{\rm eff}$, $\log g$, and [Fe/H]), we imposed Gaussian priors centered on the values reported by Perdelwitz et al. (2024) in the HARPS-RVBank. These quantities were derived from templates constructed by co-adding HARPS spectra (see Perdelwitz et al. 2024, Sect. 2.1).

A complete overview of the derived parameters is provided in Table 1, and the marginalized posterior distributions of some of the parameters are shown in Fig. 1. The resulting stellar parameters are consistent with recent literature values (e.g., Stassun et al. 2017, 2018). In particular, we find that the stellar mass is $1.06^{+0.07}_{-0.06}\,M_\odot$, compared to $1.15\,M_\odot$ in Correia et al. (2005), $1.044\,M_\odot$ in Couetdic et al. (2010), $1.27 \pm 0.12\,M_\odot$ in

[2] https://github.com/jvines/astroARIADNE
[3] https://github.com/gregreen/dustmaps

Table 2. Best Keplerian and coplanar dynamical fits to the HARPS and CORALIE RV data of HD 202206.

Orb. Param.	Keplerian fit (i = 90°)		Dynamical fit (i = 90°)		Dynamical fit (i = 51°)	
	Inner	Outer	Inner	Outer	Inner	Outer
K (m s^{-1})	562.37	43.55	562.61	43.61	562.64	43.51
P (d)	256.36	1291.02	256.28	1295.03	256.26	1298.87
e	0.426	0.130	0.426	0.177	0.426	0.180
ω (°)	161.80	86.16	161.65	81.27	161.66	82.73
M (°)	354.52	80.37	354.38	84.25	354.33	83.76
a (AU)	0.81	2.38	0.81	2.38	0.81	2.39
m ($M_{\rm J}$)	16.70	2.43	16.70	2.42	21.56	3.12
RV$_{\rm off.\ CORALIE}$ (m s^{-1})	726.39		726.82		726.71	
RV$_{\rm off.\ HAPRS\text{-}pre}$ (m s^{-1})	−15.65		−14.69		−14.59	
RV$_{\rm off.\ HAPRS\text{-}post}$ (m s^{-1})	−2.39		−3.24		−2.76	
RV$_{\rm jit.\ CORALIE}$ (m s^{-1})	6.45		6.62		6.53	
RV$_{\rm jit.\ HAPRS\text{-}pre}$ (m s^{-1})	7.21		7.26		7.31	
RV$_{\rm jit.\ HAPRS\text{-}post}$ (m s^{-1})	6.09		6.45		6.58	
rms (m s^{-1})	8.20		7.29		7.99	
ln $\mathcal{L}$	−598.02		−595.31		−594.73	

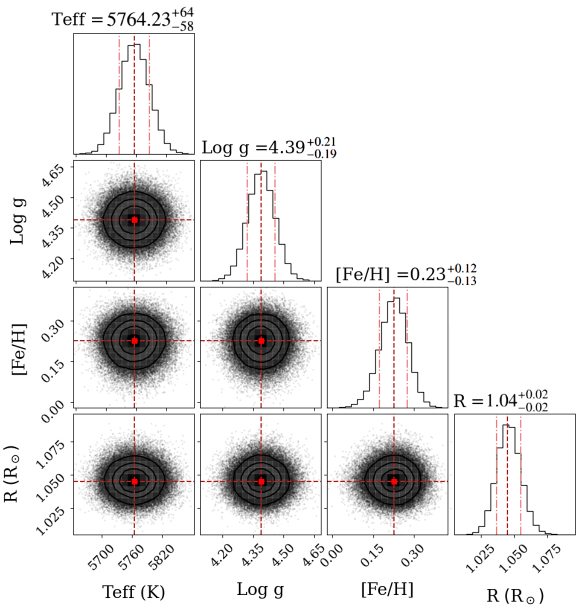

Fig. 1. Posterior probability distribution of the effective temperature ($T_{\rm eff}$), surface gravity ($\log g$), metallicity ([Fe/H]), and stellar radius (R) of the star HD 202206. The dashed red lines and squares indicate the median values and the 1σ confidence intervals.

Stassun et al. (2017), and $1.03^{+0.14}_{-0.11}\,M_\odot$ in the TESS Input Catalog (Stassun et al. 2018).

4. Orbital solutions from radial velocity and astrometric analysis

4.1. Keplerian fit

To model the orbital configuration of the system, we first assumed that the companions are on non-interacting Keplerian orbits. We adopt JD = 2451402.808 (the first CORALIE RV measurement) as the reference epoch throughout this paper. Within the Exo-Striker[4] exoplanet toolbox (Trifonov 2019), we used the Nelder–Mead (Simplex) algorithm (Nelder & Mead 1965) to optimize the likelihood function ($\ln\mathcal{L}$) coupled with a two-planet Keplerian model. The parameters that were derived through the fitting are the RV semi-amplitude (K), orbital period (P), eccentricity (e), argument of periastron (ω), mean anomaly (M), and the RV data offset (RV$_{\rm off}$) and jitter (RV$_{\rm jit}$) for each dataset. All the orbital parameters are given in the Jacobi coordinate system (Lee & Peale 2003). The best Keplerian fit to the combined dataset has $\ln\mathcal{L} = -598.02$ and is consistent with two companions of minimum masses $m_b \sin i = 16.70\,M_{\rm J}$ and $m_c \sin i = 2.43\,M_J$, orbital periods $P_b = 256.36$ days and $P_c = 1291.02$ days, and eccentricities $e_b = 0.426$ and $e_c = 0.130$ (Table 2).

4.2. Coplanar dynamical fits

For an investigation of the mutual gravitational interactions between massive companions, a description based solely on an independent Keplerian fit is inadequate. Such an approach neglects the planet–planet perturbations that can significantly modify the orbital evolution. A self-consistent N-body treatment is therefore required to properly characterize the system architecture and assess its long-term dynamical behavior. Hence, we used the best Keplerian fit as an initial guess and performed a maximum likelihood fit coupled with a self-consistent dynamical model. We first assumed a coplanar and edge-on configuration of the system ($i_b = i_c = 90°$, $\Delta\Omega = 0°$). The best-fit parameters at the reference epoch are listed in Table 2. This fit has $\ln\mathcal{L} = -595.31$, which is slightly better than the Keplerian fit, and the resulting parameters are similar to the Keplerian fit, except for the slightly longer period ($P_c = 1295.03$ days) and large eccentricity ($e_c = 0.177$) of the outer companion.

Next, we aimed to constrain the inclination of the HD 202206 system by examining the relationship between inclination and the quality of the RV fit, using specifically the log likelihood ($\ln\mathcal{L}$) and the Bayesian information criterion (BIC). These metrics provide a quantitative evaluation of the quality of the dynamical fits to the observed RV data.

[4] https://github.com/3fon3fonov/exostriker

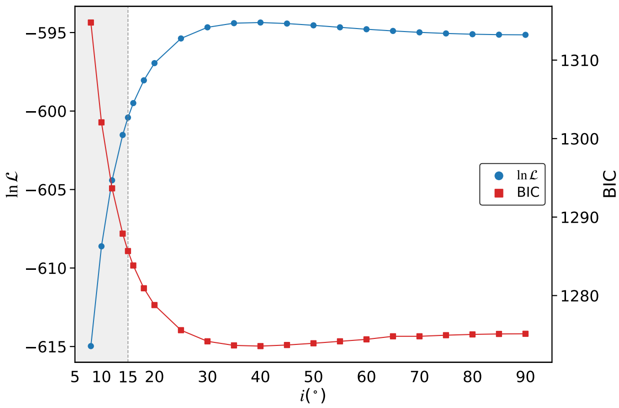

Fig. 2. Resulting ln $\mathcal{L}$ and BIC for coplanar dynamical fits as a function of the inclination (i) for the combined HARPS and CORALIE dataset. The left-hand axis is for ln $\mathcal{L}$ shown as blue circles and the right-hand axis for BIC shown in red squares. The shaded gray region illustrates the inclination that should be ruled out.

We systematically varied the system inclination (i) from 90° down to 8° and recorded the corresponding fitting statistics, ln $\mathcal{L}$ and BIC, which we present in Fig. 2. The figure shows both the ln $\mathcal{L}$ and BIC. As we can see, varying the inclination from 90° to 30° results in minimal changes to the quality of the RV fit. For inclinations below 25°, both ln $\mathcal{L}$ and BIC vary rapidly: ln $\mathcal{L}$ decreases and BIC increases, indicating a strong degradation of the model at low inclinations. The global maximum of ln $\mathcal{L}$ and the global minimum of BIC for the combined CORALIE and HARPS data occur at $i = 40°$, and we adopted those values as ln $\mathcal{L}_{\max}$ and $\mathrm{BIC}_{\min}$ when computing differential metrics.

To identify unfavorable inclination in the fitting, we defined the following metrics: $\Delta \ln \mathcal{L} = |\ln \mathcal{L}| - |\ln \mathcal{L}_{\max}|$ and $\Delta\mathrm{BIC} = \mathrm{BIC} - \mathrm{BIC}_{\min}$. The shaded gray region highlights inclinations that simultaneously breach the $\Delta \ln \mathcal{L} > 7$ and $\Delta\mathrm{BIC} > 10$ thresholds (Kass & Raftery 1995; Trifonov et al. 2022). The above tests reveal that an inclination ≤15° is strongly disfavored by the RV fits, contradicting the low-inclination solution reported by Benedict & Harrison (2017).

4.3. Astrometric analysis

To further constrain the inclination and the three-dimensional geometry of the HD 202206 system, we made use of the *Gaia* Data Release 3 (DR3) astrometry together with the RV posteriors from a nested sampling run of the Keplerian fit. We modeled the astrometric orbits of the two companions under a coplanar assumption with the same inclinations and longitudes of the ascending nodes. We used three constraints to fit the orbits: the astrometric jitter around the best fit in the *Gaia* DR3 catalog (assuming this is exclusively due to the companions) as well as the two proper motion anomalies in right ascension and declination. The latter are derived from the differences between the catalog proper motions from Hipparcos (van Leeuwen 2007) and *Gaia* DR3, respectively, and the long-term proper motion computed from the positional difference between *Hipparcos* and *Gaia* DR3, as given by Kervella et al. (2022). Because the *Gaia* DR3 astrometric jitter includes epoch-astrometry outliers that have not yet been removed, it should be regarded as an upper limit on the true companion- induced signal; consequently, the inclination derived from the astrometric jitter should be interpreted as a lower limit; the true absolute inclination may be higher than the nominal value inferred here.

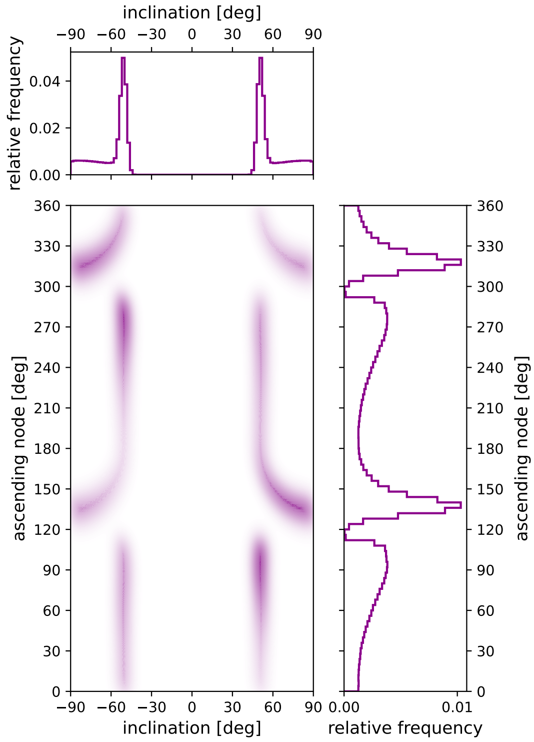

Fig. 3. Posterior probability distributions for the orbital inclination (i) and the longitude of the ascending node (Ω) derived from the nested sampling analysis using astrometric constraints. *Center*: joint density distribution. *Top and right*: marginalized one-dimensional probability density functions. The inclination peaks at approximately ±50.7°, and the longitude of the ascending node presents corresponding peaks at 137.5° and 317.5°.

Briefly, we fitted the astrometric orbits by drawing from the spectroscopic posteriors 1000 times. For each of those 1000 combinations of spectroscopic parameters, we computed the log likelihood by combining the three different constraints from the astrometry and performed a nested sampling run using DYNESTY (Speagle 2020), in order to obtain the best inclination and ascending node. Finally, we obtained a single posterior that takes both the errors in the spectroscopic parameters and in the astrometric constraints into account. In order to simulate the astrometric orbit and compare the resulting astrometric excess jitter with that reported in *Gaia* DR3, we obtained the time and scan direction of the individual *Gaia* abscissa measurements from the *Gaia* Observation Forecast Tool GOST[5], and we estimated the accuracy of each *Gaia* measurement from the final catalog accuracy and the number of individual measurements that went into it. We also fitted positions, proper motions, and parallax terms to our simulated abscissae so that the simulated astrometric excess scatter does not contain terms that would have been subsumed into those parameters.

Figure 3 shows the posterior distribution of the inclination and ascending nodes of the astrometric analysis, and Table 3 provides the corresponding values of the resulting inclination and ascending nodes. The orbital inclination derived from our simulations converges consistently to values near 51°. The posterior distributions exhibit a sharp and asymmetric peak, with a best-fit value of $50.7^{+25.8}_{-1.4}$ degrees and a long shallow tail toward higher inclinations. The narrow widths of the posterior

[5] https://gaia.esac.esa.int/gost/

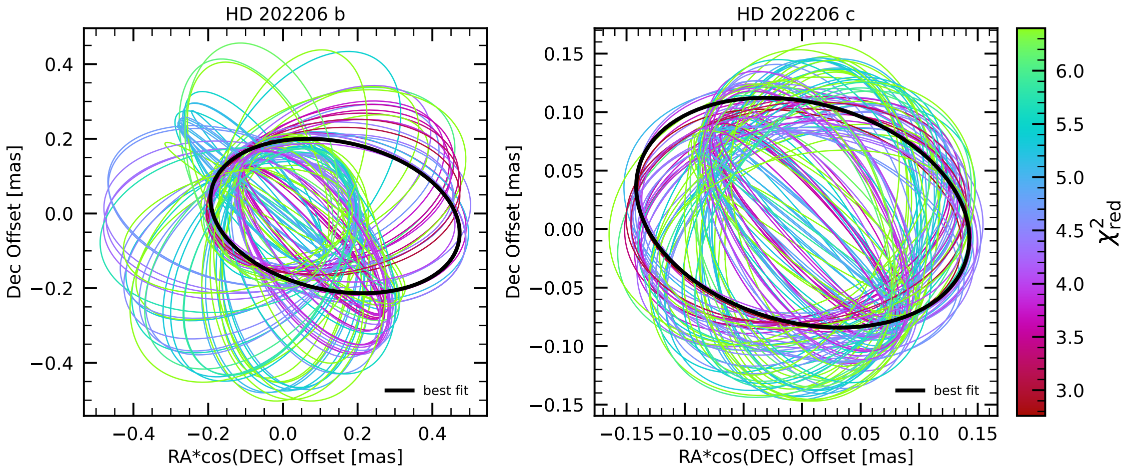

Fig. 4. Astrometric orbital simulations for HD 202206 b (*left*) and HD 202206 c (*right*) constrained by astrometric data. The simulations utilize the proper motion anomalies in right ascension and declination, defined as the difference between the HIPPARCOS and *Gaia* proper motion vectors, as reported by Kervella et al. (2022). The curves represent a sample of orbital solutions drawn from the posterior distribution, color-coded by the reduced chi-squared statistic (χ^2_{red}) of the fit to the astrometric constraints. The solid black ellipses indicate the best-fitting orbital solutions corresponding to the minimum χ^2_{red}.

Table 3. Inclination and ascending node of the HD 202206 system from astrometric analysis.

Parameter	Value[(a)]
Inclination (positive)	$50.7^{+25.8}_{-1.4}$
Inclination (negative)	$-50.7^{+1.4}_{-25.8}$
Ascending node (small)	$137.5^{+8.6}_{-84.9}$
Ascending node (large)	$317.5^{+8.6}_{-85.0}$

Notes. [(a)]Posterior modes with 1σ confidence intervals.

peaks indicate that the inclination is well constrained once the spectroscopic and astrometric data are combined.

Together with the inclination, the longitude of the ascending node is also restricted to two groups of solutions around 138° and 318°. Figure 4 illustrates the fitted astrometric orbits of the two companions in the HD 202206 system.

4.4. Coplanar dynamical fit with i = 51°

Since our astrometric analysis showed that the orbital inclination is strongly constrained to about 51°, we derived the best coplanar inclined fit by fixing the inclination to 51° and redoing the dynamical fit to the CORALIE and HARPS RV data. Figure 5 shows the best coplanar $i = 51°$ dynamical fit, and the parameters derived for this fit are listed in Table 2. Our best-fit dynamical solution yields actual masses of 21.56 M_{J} and 3.12 M_{J} for the inner and outer companions, respectively. The corresponding orbital periods are 256.26 days and 1298.87 days, with eccentricities of 0.426 and 0.180, respectively, at the reference epoch.

5. Orbital evolution

5.1. Evolution of the best i=51° fit

In this section, we begin by presenting the evolution of key orbital parameters for the HD 202206 system. The integrator we used for our *N*-body simulation is the Wisdom–Holman symplectic integrator (Wisdom & Holman 1991) implemented in the EXO-STRIKER. Starting from the initial observational epoch JD = 2451402.808 (the first CORALIE data point), we performed the orbital integration for 1 million years using a fixed time step of 2 days, which gives roughly 128 integration steps per orbit of the inner companion.

Given that the orbital period ratio of the companions is approximately 5:1, we further monitored both the evolution of the secular apsidal angle ($\Delta\varpi = \varpi_b - \varpi_c$) and the evolution of all five resonance angles, defined as follows:

$$\theta_1 = \lambda_b - 5\lambda_c + 4\varpi_b, \quad (1)$$

$$\theta_2 = \lambda_b - 5\lambda_c + 3\varpi_b + \varpi_c, \quad (2)$$

$$\theta_3 = \lambda_b - 5\lambda_c + 2\varpi_b + 2\varpi_c, \quad (3)$$

$$\theta_4 = \lambda_b - 5\lambda_c + \varpi_b + 3\varpi_c, \quad (4)$$

$$\theta_5 = \lambda_b - 5\lambda_c + 4\varpi_c, \quad (5)$$

where $\varpi_{b,c} = \Omega_{b,c} + \omega_{b,c}$ is the longitude of periastron and $\lambda_{b,c} = M_{b,c} + \varpi_{b,c}$ is the mean longitude, with $\Omega_{b,c}$, $\omega_{b,c}$, and $M_{b,c}$ being the longitude of the ascending node, the argument of periastron, and the mean anomaly, respectively. Note that $\Omega_b = \Omega_c = 0°$ for our coplanar fits.

Figure 6 shows a 10 kyr segment drawn from the 1 Myr integration of the best coplanar $i = 51°$ fit. Over the entire 10 kyr window, the semimajor axes are effectively constant, showing only small, regular variations. The inner companion remains around $a_b \approx 0.80$ AU, and the outer companion remains near $a_c \approx 2.40$ AU. The eccentricities display coherent, periodic variations on a timescale of ≈290 yr. The eccentricity of the inner companion exhibits small-amplitude oscillations with $e_b \approx 0.41$–0.43 (mean ≈ 0.42). The outer companion shows larger cyclic variations with $e_c \approx 0.06$–0.22 (mean ≈ 0.15–0.16) over each cycle. These eccentricity oscillations are regular and repeat across the entire 1 Myr interval. The apsidal difference ($\Delta\varpi$) circulates through the full ±180° range on the same timescale of ≈290 yr (green), indicating that the orbits are not locked in an aligned apsidal configuration. Of the five resonant angles, only θ_4 clearly librates around 0°, with a semi-amplitude of approximately

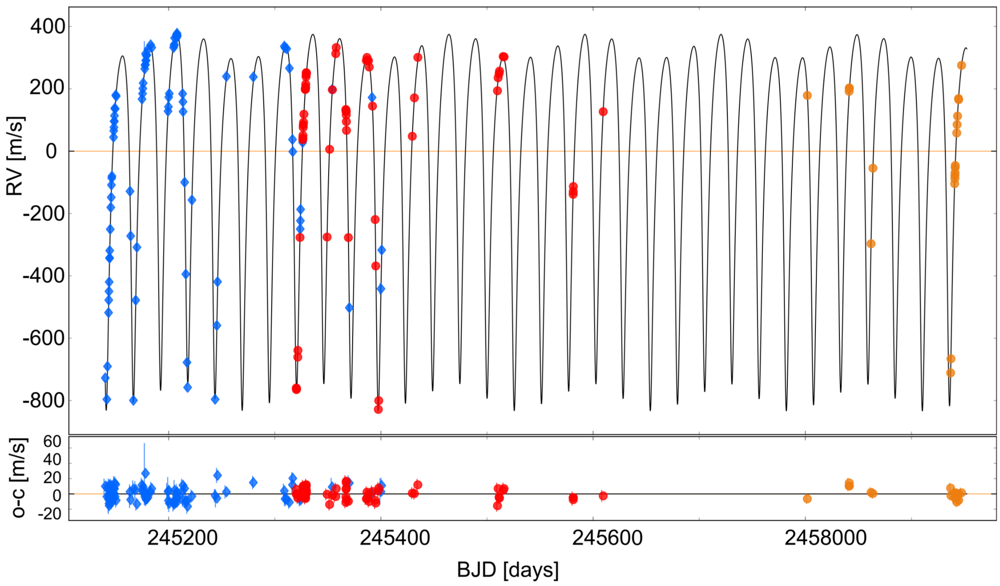

Fig. 5. *Top*: best coplanar $i = 51°$ dynamical fit to the CORALIE (blue), HARPS-pre (red), and HARPS-post (orange) RV data of HD 202206. *Bottom*: residuals around the best fit.

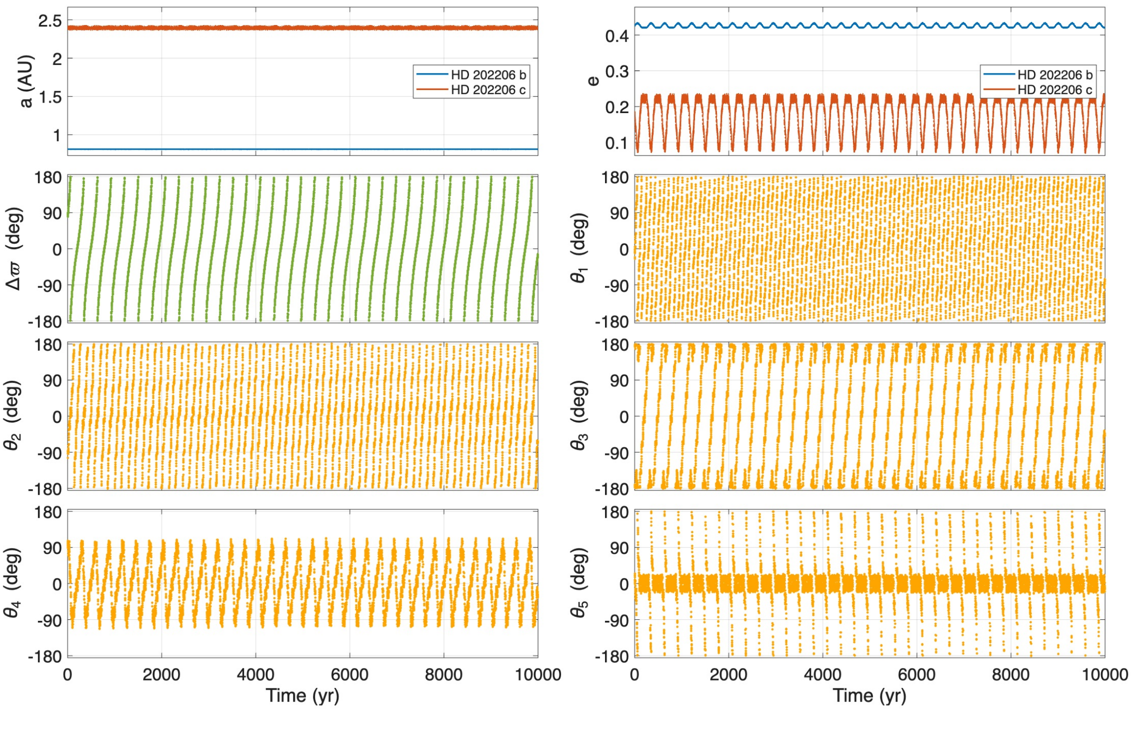

Fig. 6. Orbital evolution of the best coplanar inclined ($i = 51°$) dynamical fit, shown for 10 kyr from the N-body simulation. The panels display the semimajor axes a_b (blue) and a_c (red), the eccentricities e_b (blue) and e_c (red), the secular apsidal difference, $\Delta\varpi$ (green), and the resonant angles θ_1, θ_2, θ_3, θ_4, and θ_5 (orange).

$\pm$100–120°. The other angles, θ_1, θ_2, θ_3, and θ_5, circulate through the full $\pm 180°$ range. The libration period seen in θ_4 is consistent with the dominant period of the eccentricity oscillations and the circulation of $\Delta\varpi$.

5.2. Nested sampling

We employed dynamic nested sampling (Skilling 2004; Higson et al. 2019) to perform posterior inference for the HD 202206 system. We employed the dynamic nested sampling package DYNESTY (Speagle 2020), which explores the parameter space around the best-fit solution through random walks and provides a well-defined convergence criterion based on the remaining log-evidence, $\Delta \ln Z$. This enables a robust assessment of orbital architecture and associated dynamical behaviors, thereby informing the long-term stability and plausible formation pathways of the system. Each fitting parameter was sampled with 100 live points, and the runs were terminated once the remaining log-evidence ($\Delta \ln Z$) dropped below 0.001. These settings ensure a robust convergence of dynamic nested sampling. The median

Table 4. Posterior estimates (median and 1σ region) for coplanar edge-on and inclined (i = 51°) dynamical fits.

	N-body(i = 51°)		N-body(i = 90°)		Adopted priors	
Orb. param.	Inner	Outer	Inner	Outer	Inner	Outer
K (m s^{-1})	$562.58^{+1.35}_{-1.36}$	$43.04^{+1.17}_{-1.16}$	$560.87^{+3.04}_{-0.31}$	$44.02^{+0.05}_{-2.20}$	$\mathcal{U}$(500, 600)	$\mathcal{U}$(40,50)
P (d)	$256.26^{+0.03}_{-0.03}$	$1299.22^{+3.21}_{-2.76}$	$256.32^{+0.01}_{-0.08}$	$1294.31^{+6.59}_{-0.94}$	$\mathcal{U}$(200,300)	$\mathcal{U}$(1200,1400)
e	$0.426^{+0.002}_{-0.002}$	$0.171^{+0.021}_{-0.025}$	$0.427^{+0.001}_{-0.002}$	$0.149^{+0.039}_{-0.009}$	$\mathcal{U}$(0.2,0.6)	$\mathcal{U}$(0.01,0.3)
ω (°)	$161.64^{+0.29}_{-0.28}$	$84.73^{+6.53}_{-4.05}$	$161.82^{+0.11}_{-0.46}$	$82.86^{+11.20}_{-3.16}$	$\mathcal{U}$(0,360)	$\mathcal{U}$(0,360)
Ma (°)	$354.33^{+0.29}_{-0.29}$	$81.97^{+6.53}_{-6.51}$	$345.38^{+0.27}_{-0.32}$	$83.60^{+2.52}_{-10.45}$	$\mathcal{U}$(0,360)	$\mathcal{U}$(0,360)
a (AU)	$0.81^{+0.01}_{-0.02}$	$2.39^{+0.04}_{-0.05}$	$0.82^{+0.00}_{-0.02}$	$2.40^{+0.03}_{-0.06}$	(derived)	
m ($M_{\rm J}$)	$21.55^{+0.80}_{-0.81}$	$3.09^{+0.14}_{-0.14}$	$16.89^{+0.42}_{-0.83}$	$2.49^{+0.00}_{-0.20}$	(Derived)	
RV$_{\rm off.\ CORALIE}$ (m s^{-1})	$725.94^{+1.92}_{-0.27}$		$726.60^{+1.40}_{-0.83}$		$\mathcal{U}$(-1000,1000)	
RV$_{\rm off.\ HAPRS\text{-}pre}$ (m s^{-1})	$-14.21^{+0.66}_{-1.73}$		$-16.56^{+2.81}_{-0.42}$		$\mathcal{U}$(-100,100)	
RV$_{\rm off.\ HAPRS\text{-}post}$ (m s^{-1})	$1.81^{+0.71}_{-7.98}$		$-2.38^{+3.70}_{-4.20}$		$\mathcal{U}$(-100,100)	
RV$_{\rm jit.\ CORALIE}$ (m s^{-1})	$6.80^{+0.59}_{-1.29}$		$7.42^{+0.01}_{-1.93}$		$\mathcal{J}$(0.1,50)	
RV$_{\rm jit.\ HAPRS\text{-}pre}$ (m s^{-1})	$8.39^{+0.08}_{-1.53}$		$7.50^{+0.96}_{-0.64}$		$\mathcal{J}$(0.1,50)	
RV$_{\rm jit.\ HAPRS\text{-}post}$ (m s^{-1})	$5.82^{+2.79}_{-0.13}$		$8.44^{+0.22}_{-2.50}$		$\mathcal{J}$(0.1,50)	

Notes. The adopted priors are listed in the right-most columns, with $\mathcal{U}$ and $\mathcal{J}$ denoting uniform and Jeffrey's priors, respectively.

Table 5. Stability and libration ratio of θ_4 for different inclinations.

Inclination (i)	Stability (%)	Libration ratio of θ_4 (%)
90°	99.96	76.73
51°	99.78	88.10

Notes. From 5000 subsamples integrated up to 10 Myr.

and 1σ range of the posteriors of the fitted parameters for the coplanar edge-on (i = 90°) and inclined (i = 51°) dynamical fits are listed in Table 4, and the posterior probability distributions of the orbital parameters for the coplanar i = 51° dynamical fit are shown in Fig. 7.

5.3. Orbital stability and libration of θ_4

We used N-body simulations performed with the Wisdom-Holman method (Wisdom & Holman 1991) up to a maximum of 10 Myr to analyze the statistics of long-term dynamics from 5000 subsamples randomly extracted from the nested sampling posterior distribution of the coplanar edge-on (i = 90°) and inclined (i = 51°) fits for the HD 202206 system. A subsample is defined as unstable if $e > 0.9$ or the semimajor axis changes by more than 60% from its initial value for either planet. Otherwise, it is considered stable. Thus, stability is the fraction of stable subsamples, while the libration rate of θ_4 is the fraction of subsamples in which θ_4 exhibits libration ($\Delta\theta_4 < 170°$). For both inclinations, none of the subsamples show librations of θ_1, θ_2, θ_3, or θ_5. The results of this analysis are presented in Table 5. For i = 90°, we find that 76.7% of the subsamples exhibit a libration of θ_4 about 0°. The libration ratio of θ_4 increases to 88.1% for i = 51°. Figure 8 presents the distributions of the mean value of θ_4 and the semi-amplitude ($\Delta\theta_4$) about the mean for the i = 51° subsamples. The librating cases show large amplitude libration, with the peak in the distribution of $\Delta\theta_4$ at ∼110°, while the circulating cases shift the median of $\Delta\theta_4$ to a slightly larger value of 116.°7. It can be seen that the stable fraction is maintained above 99% for both inclinations, indicating that dynamical stability does not provide an additional constraint on the libration or circulation of θ_4. We also verified that the stable fraction and the libration ratio are not sensitive to the maximum integration time. They change by ∼1% only when we integrate a smaller set of 2000 subsamples from the i = 51° posterior up to 100 Myr. Based on these findings, we conclude that the HD 202206 system is in a broadly stable region of the parameter space and that it is most likely in the 5:1 MMR with only θ_4 librating.

6. Discussion

6.1. Dominance of resonance angle θ_4

For a system with two companions b and c, which are on coplanar inner and outer orbits, respectively, the disturbing function for their gravitational interaction can be written as (Murray & Dermott 1999; Mardling 2013)

$$\mathcal{R} = \sum_{m=0}^{\infty} \sum_{n'=-\infty}^{\infty} \sum_{n=-\infty}^{\infty} \mathcal{R}_{mn'n} \cos\phi_{mn'n}, \tag{6}$$

where the harmonic angle

$$\phi_{mn'n} = n'\lambda_b - n\lambda_c + (m-n')\varpi_b - (m-n)\varpi_c. \tag{7}$$

For the n:n' commensurability, the order of the resonance is $n - n'$, and there are $n - n' + 1$ resonance angles ($\phi_{mn'n}$) with $m = 1, \ldots, n - n' + 1$. When the companions are far apart and the semimajor axis ratio ($\alpha = a_b/a_c$) is small, the strongest MMRs are the n:1 resonances with $n' = 1$ (Gallardo 2006; Mardling 2008).

In the HD 202206 system, we find that only the 5:1 resonance angle with $m = 2$ (i.e., $\phi_{2,1,5} = \theta_4 = \lambda_b - 5\lambda_c + \varpi_b + 3\varpi_c$) librates with a large amplitude. The remaining four 5:1 resonance angles circulate together with the apsidal angle $\Delta\varpi = \varpi_b - \varpi_c$. The

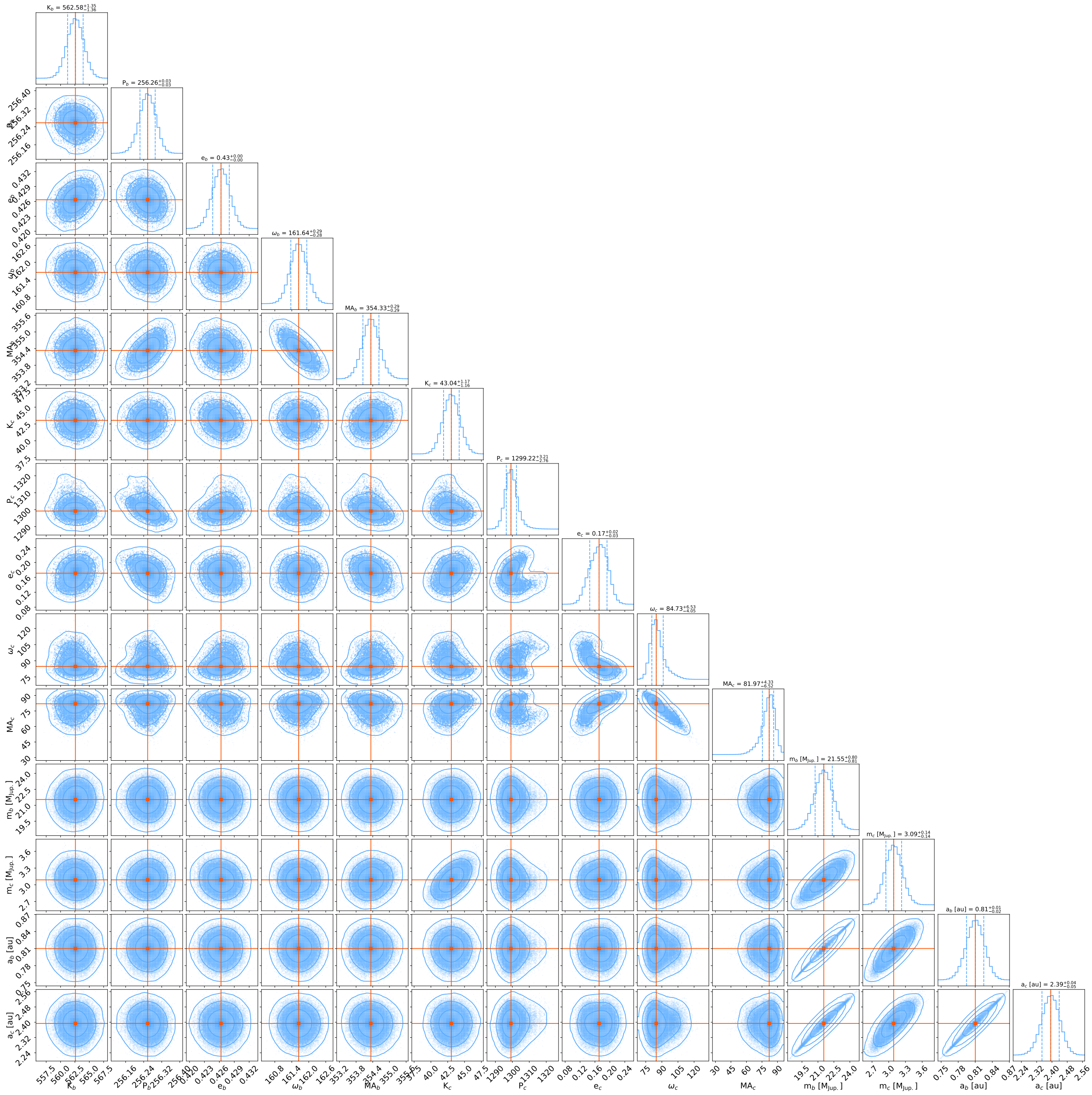

Fig. 7. Posterior probability distributions of the orbital parameters of HD 202206 from the nested sampling analysis of the coplanar inclined (i = 51°) dynamical fit to the combined HARPS and CORALIE dataset. The solid red lines indicate the median of each fitted parameter, and the 1σ confidence intervals are indicated by the vertical dashed blue lines. The blue contours in the two-dimensional panels indicate the 1σ, 2σ, and 3σ confidence intervals.

6:1 MMR in the ν Oph system behaves differently, with all of its associated resonance angles exhibiting stable libration. However, the angle with $m = 2$ (i.e., $\phi_{2,1,6} = \lambda_b - 6\lambda_c + \varpi_b + 4\varpi_c$) also shows the smallest libration amplitude (Quirrenbach et al. 2019). In addition, in his study of planetary orbits around the primary star of the HD 59686 binary system, Wong (2018) found that, for the orbits that are stabilized by n:1 MMRs with n~40, the angle $\phi_{2,1,n}$ (with $m = 2$) also exhibits the smallest libration amplitude. This general behavior that the $m = 2$ resonance angle is the dominant angle for n:1 MMRs requires an explanation.

Previous studies have shown, through an appropriate canonical transformation, that the first-order n:$(n-1)$ MMR problem can be reduced to an integrable one-degree-of-freedom problem with a single mixed resonance angle (Sessin & Ferraz-Mello 1984; Henrard et al. 1986; Wisdom 1986; Batygin & Morbidelli 2013; Nesvorný & Vokrouhlický 2016; Petit et al. 2020). For higher-order resonances with $n/n' < 2$ or $P_c/P_b < 2$, Hadden (2019) has shown that a near-symmetry of the disturbing function also allows the problem to be approximated as an integrable one-degree-of-freedom problem with a single mixed resonance angle. However, this reduction does not apply to n:1 resonances with $n > 2$.

For high-order n:1 MMRs where n is large and α is small, an alternative approach is to expand the disturbing function in spherical harmonics or powers of α (Mardling 2013):

$$\mathcal{R}_{mn'n} = \frac{G\mu_i m_c}{a_c} \sum_{l=l_{\min},2}^{\infty} \zeta_m c_{lm}^2 \mathcal{M}_l \alpha^l X_{n'}^{l,m}(e_b) X_n^{-(l+1),m}(e_c), \qquad (8)$$

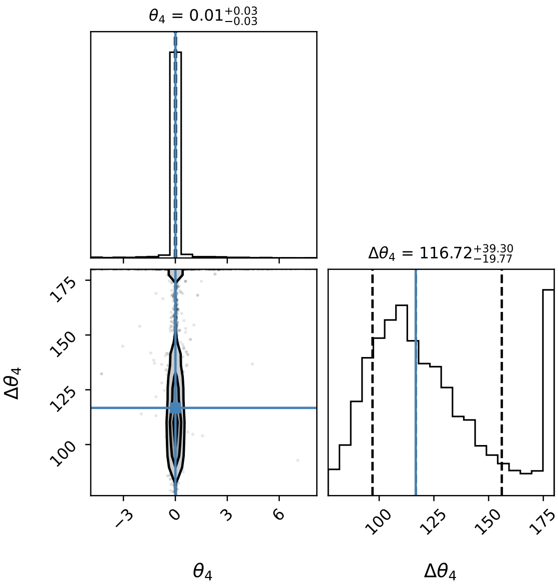

Fig. 8. Distributions of the mean value of θ_4 and the semi-amplitude, $\Delta\theta_4$, from a 10 Myr integration of 5000 subsamples extracted from the posterior of the coplanar inclined ($i = 51^\circ$) dynamical fit to the combined CORALIE and HARPS dataset of HD 202206. The vertical solid blue lines indicate the median of each parameter, and the vertical dashed black lines indicate the 1σ confidence intervals. The black contours in the two-dimensional panels indicate the 1σ, 2σ, and 3σ confidence intervals.

where $X^{l,m}_{n'}(e_b)$ and $X^{-(l+1),m}_{n}(e_c)$ are Hansen coefficients and $l_{\min} = 3$ for $m = 1$ and $l_{\min} = m$ for $m \geq 2$ (see Mardling 2013 for the definitions of the other variables in Eq. (8)). For given n and n', only $R_{mn'n}$ with $m = 2$ includes a term with the lowest power of α, which is the quadrupole term with $l = 2$ or α^2. Other $R_{mn'n}$ with $m \neq 2$ include only terms of order α^3 or higher. This explains why the $m = 2$ resonance angle is usually the dominant one for high-order n:1 MMRs (see also Mardling 2008, 2013).

6.2. Formation and migration scenario

The existence of a MMR between two companions requires convergent migration and resonance capture (Goldreich 1965; Murray & Dermott 1999). High-order MMRs are generally difficult to assemble and maintain because the width of a resonance decreases with increasing resonance order (Murray & Dermott 1999; Mardling 2008, 2013). Capture into high-order MMRs probably requires slow migration and nonzero initial eccentricities.

The 5:1 MMR in HD 202206 and the 6:1 MMR in ν Oph are the only high-order n:1 resonances confirmed to date for systems with substellar companions beyond the Solar System. They are similar in having a brown dwarf inner companion, but they differ in other respects. The ν Oph system involves two companions of comparable masses ($m_b \sin i = 22.2\,M_J$ and $m_c \sin i = 24.7\,M_J$) and eccentricities ($e_b = 0.12$ and $e_c = 0.18$), with all six resonance angles librating. Quirrenbach et al. (2019) have argued that this configuration is most likely consistent with a scenario in which the two brown dwarfs formed and migrated in a disk around the star. The HD 202206 system is a hierarchical system that hosts an inner brown dwarf with $m_b = 21.6\,M_J$ and an outer giant planet with $m_c = 3.1\,M_J$. There are two plausible formation scenarios: (1) the formation and migration of both the brown dwarf and the giant planet in a circumstellar disk (as proposed for ν Oph) or (2) the formation of the star–brown dwarf binary, followed by the formation and migration of the giant planet in a circumbinary disk. In the context of the second scenario, it is interesting to note that simulations of planet migration in circumbinary disks around binary stars have shown capture into MMRs such as 4:1 and 5:1 (e.g., Nelson 2003; Kley & Haghighipour 2014; Zoppetti et al. 2018). However, since none of the observed circumbinary planets are in a n:1 resonance with the binary, these works have proposed either a wider disk cavity to stop migration before MMR capture or subsequent evolution out of the MMR due to tides or scattering. Since the companions in HD 202206 are in 5:1 MMRs, these additional processes must be ineffective, which could be due to the low mass and long period of the inner companion compared to the secondary stars of binaries with circumbinary planets.

The current dynamical architecture of the HD 202206 system can be used to constrain the formation scenarios. The large mass ratio $m_b/m_c = 6.9$ of the HD 202206 companions means that it would be difficult to increase e_b significantly after resonance capture, and the inner brown dwarf may be required to have a rather high eccentricity (comparable to its current value $e_b = 0.43$) before resonance capture. The large amplitude libration of only θ_4 may be a consequence of the high e_b before resonance capture. A detailed exploration of the formation and migration scenarios of HD 202206 and ν Oph, including the specific constraints on initial parameters and migration rates, will be presented in our forthcoming study (Cao et al., in prep.).

7. Summary

We have presented a comprehensive dynamical analysis of the HD 202206 system that we carried out by combining RV data from CORALIE and HARPS with astrometric constraints from *Gaia* DR3 and HIPPARCOS. The inclusion of astrometric proper motion anomalies and jitter constraints resolved the previous ambiguity regarding the system orientation and constrained the orbital inclination to $50.7^{+25.8}_{-1.4}$ degrees. This result, as well as the poor quality of the dynamical fit to the RV data at low inclinations, allows us to rule out the low-inclination solution previously proposed by Benedict & Harrison (2017) and confirms that the inner companion, HD 202206 b, possesses a true mass of 21.6 M_J in the brown dwarf regime, distinct from the planetary mass 3.1 M_J of the outer companion. The derived coplanar inclined ($i = 51^\circ$) solution yields orbital periods of 256.26 and 1299 days, with significant eccentricities of 0.426 and 0.180 for the inner and outer companions, respectively.

Our numerical N-body simulations confirm that the system is dynamically stable and is most likely in the 5:1 MMR. A detailed inspection of the resonance angles reveals that only the angle $\theta_4 = \lambda_b - 5\lambda_c + \varpi_b + 3\varpi_c$ is librating with a large amplitude; the other resonance angles circulate. The dominance of the angle involving one ϖ_b for high-order n:1 MMRs is due to the fact that the quadrupole term in the disturbing function contributes only to the resonance term involving this angle.

The existence of a brown dwarf and a giant planet in such a high-order MMR strongly favors formation scenarios involving disk-induced migration. This could involve either the formation and migration of both companions in a circumstellar disk or the formation and migration of the giant planet in a circumbinary disk after the formation of the star–brown dwarf binary. The former scenario would imply that brown dwarfs can originate from planet-like formation channels within a circumstellar disk rather than solely through cloud fragmentation processes, as suggested previously for the ν Oph system, which consists of two brown-dwarf companions in a 6:1 MMR (Quirrenbach et al. 2019). The constraints on the formation history of HD 202206 from its observed dynamical state will be investigated in detail in our future work.

Acknowledgements. Y.C. and M.H.L. were supported in part by the Hong Kong RGC grant 17309323. T.T. and S.S. acknowledge support by the Bulgarian National Science Fund BNSF program "VIHREN-2021" project No. KP-06-DV/5/15.12.2021.

References

Allard, F., Homeier, D., & Freytag, B. 2012, Philos. Trans. Roy. Soc. Lond. A, 370, 2765
Bailer-Jones, C. A. L., Rybizki, J., Fouesneau, M., Demleitner, M., & Andrae, R. 2021, AJ, 161, 147
Batygin, K., & Morbidelli, A. 2013, A&A, 556, A28
Benedict, G. F., & Harrison, T. E. 2017, ApJ, 153, 258
Castelli, F., & Kurucz, R. L. 2003, in IAU Symposium, 210, Modelling of Stellar Atmospheres, eds. N. Piskunov, W. W. Weiss, & D. F. Gray, A20
Choi, J., Dotter, A., Conroy, C., et al. 2016, ApJ, 823, 102
Correia, A. C. M., Udry, S., Mayor, M., & et al. 2005, A&A, 440, 751
Correia, A. C. M., Udry, S., Mayor, M., & et al. 2009, A&A, 496, 521
Couetdic, J., Laskar, J., Correia, A. C. M., Mayor, M., & Udry, S. 2010, A&A, 519, A10
Desort, M., Lagrange, A.-M., Galland, F., et al. 2008, A&A, 491, 883
Dotter, A. 2016, ApJS, 222, 8
Gaia Collaboration (Vallenari, A., et al.) 2023, A&A, 674, A1
Gallardo, T. 2006, Icarus, 184, 29
Goldreich, P. 1965, MNRAS, 130, 159
Green, G. M. 2018, J. Open Source Softw., 3, 695
Hadden, S. 2019, ApJ, 158, 238
Hauschildt, P. H., Allard, F., & Baron, E. 1999, ApJ, 512, 377
Henrard, J., Lemaître, A., Milani, A., & Murray, C. D. 1986, Celest. Mech., 38, 335
Higson, E., Handley, W., Hobson, M., & Lasenby, A. 2019, Statist. Comput., 29, 891
Høg, E., Fabricius, C., Makarov, V. V., et al. 2000, A&A, 355, L27
Husser, T. O., Wende-von Berg, S., Dreizler, S., et al. 2013, A&A, 553, A6
Jenkins, J., Tuomi, M., Brasser, R., Ivanyuk, O., & Murgas, F. 2013, ApJ, 771
Kass, R. E., & Raftery, A. E. 1995, J. Am. Statist. Assoc., 90, 773
Kervella, P., Arenou, F., & Thévenin, F. 2022, A&A, 657, A7
Kley, W., & Haghighipour, N. 2014, A&A, 564, A72
Kley, W., Peitz, J., & Bryden, G. 2004, A&A, 414, 735
Kurucz, R. 1993, Robert Kurucz CD-ROM, 13
Laskar, J., & Correia, A. C. M. 2009, A&A, 496, L5
Lee, M. H., & Peale, S. J. 2002, ApJ, 567, 596
Lee, M., & Peale, S. 2003, ApJ, 592
Luque, R., Trifonov, T., Reffert, S., et al. 2019, A&A, 631, A136
Ma, B., & Ge, J. 2014, MNRAS, 439, 2781
Marcy, G. W., Butler, R. P., Fischer, D., et al. 2001, ApJ, 556, 296
Mardling, R. A. 2008, in Lecture Notes in Physics, 760, The Cambridge *N*-Body Lectures (Springer Berlin Heidelberg), 59
Mardling, R. A. 2013, MNRAS, 435, 2187
Mayor, M., Udry, S., Naef, D., et al. 2004, A&A, 415, 391
Migaszewski, C., Goździewski, K., & Panichi, F. 2016, MNRAS, 465, 2366
Mordasini, C., Alibert, Y., & Benz, W. 2009, A&A, 501, 1139
Murray, C. D., & Dermott, S. F. 1999, Solar System Dynamics (Cambridge: Cambridge University Press)
Nelder, J. A., & Mead, R. 1965, Comput. J., 7, 308
Nelson, R. P. 2003, MNRAS, 345, 233
Nesvorný, D., & Vokrouhlický, D. 2016, ApJ, 823, 72
Papaloizou, J. C. B., & Terquem, C. 2006, Rep. Progr. Phys., 69, 119
Perdelwitz, V., Trifonov, T., Teklu, J. T., Sreenivas, K. R., & Tal-Or, L. 2024, A&A, 683, A125
Petit, A. C., Petigura, E. A., Davies, M. B., & Johansen, A. 2020, MNRAS, 496, 3101
Queloz, D., Mayor, M., Weber, L., et al. 2000, A&A, 354, 99
Quirrenbach, A., Trifonov, T., Lee, M., & Reffert, S. 2019, A&A, 624, A18
Sato, B., Omiya, M., Harakawa, H., et al. 2012, PASJ, 64
Schlafly, E. F., & Finkbeiner, D. P. 2011, ApJ, 737, 103
Sessin, W., & Ferraz-Mello, S. 1984, Celest. Mech., 32, 307
Skilling, J. 2004, in American Institute of Physics Conference Series, 735, Bayesian Inference and Maximum Entropy Methods in Science and Engineering: 24th International Workshop on Bayesian Inference and Maximum Entropy Methods in Science and Engineering, eds. R. Fischer, R. Preuss, & U. V. Toussaint (AIP), 395
Speagle, J. S. 2020, MNRAS, 493, 3132
Stassun, K. G., Collins, K. A., & Gaudi, B. S. 2017, AJ, 153, 136
Stassun, K. G., Oelkers, R. J., Pepper, J., et al. 2018, AJ, 156, 102
Tinney, C. G., Butler, R. P., Marcy, G. W., et al. 2006, ApJ, 647, 594
Trifonov, T., Reffert, S., Tan, X., Lee, M. H., & Quirrenbach, A. 2014, A&A, 568, A64
Trifonov, T., Kürster, M., Zechmeister, M., et al. 2017, A&A, 602, L8
Trifonov, T. 2019, The Exo-Striker: Transit and radial velocity interactive fitting tool for orbital analysis and *N*-body simulations, Astrophysics Source Code Library [record ascl:1906.004]
Trifonov, T., Tal-Or, L., Zechmeister, M., et al. 2020, A&A, 636, A74
Trifonov, T., Wollbold, A., Kürster, M., et al. 2022, AJ, 164, 156
van Leeuwen, F. 2007, A&A, 474, 653
Vines, J. I., & Jenkins, J. S. 2022, MNRAS, 513, 2719
Vogt, S. S., Butler, R. P., Marcy, G. W., et al. 2005, ApJ, 632, 638
Wisdom, J. 1986, Celest. Mech., 38, 175
Wisdom, J., & Holman, M. J. 1991, AJ, 102, 1528
Wong, K.-H. 2018, M. Phil. thesis, The University of Hong Kong, Hong Kong
Zoppetti, F. A., Beaugé, C., & Leiva, A. M. 2018, MNRAS, 477, 5301